JOURNAL OF COMPUTATIONAL PHYSICS 66, 99–131 (1986)

A Relaxation Approach to Patched-Grid Calculations with the Euler Equations

MAN MOHAN RAI

NASA Ames Research Center, Moffett Field, California

Received March 11, 1985; revised December 12, 1985

A conservative zonal-boundary condition that was used with explicit integration schemes is extended to implicit, upwind, relaxation schemes; in particular to the Osher scheme. The rate of convergence was found to increase considerably with the use of the implicit, relaxation-zonal-scheme when compared to the explicit scheme. The relaxation-zonal scheme has also been used in a time-accurate mode. Results demonstrating the time accuracy of the scheme and the feasibility of performing calculations in cases where some parts of the given system move relative to others (e.g., rotor-stator configurations) are presented.

INTRODUCTION

The "zonal" or "patched-grid" approach is one in which calculations are performed on several grids that are patched together at zonal interfaces. This makes the solution of geometrically complex problems a relatively straightforward task. The solution is obtained by (1) dividing the complex region into several simpler subregions or zones, (2) generating grids for each zone independently using existing grid generation schemes, and (3) solving the equations of motion in each zone. The interior points of each zone are updated using a standard integration scheme, and the points on the zonal interfaces are updated using a zonal-boundary condition. In addition to simplifying the complex geometry problem, the zonal or patch-grid approach has the following advantages: (1) grid points can be selectively added to flow regions requiring fine grids to resolve rapidly changing flow variables, and (2) data corresponding to a single zone only needs to reside in the main memory of the computer at any give time; the remaining data may reside on tape or disk (this alleviates the problem of limited computer storage).

A zonal-boundary scheme is developed for the Euler equations cast in generalized coordinates in Refs. [1] and [2]. It is fully conservative and permits distortion-free movement of flow discontinuities such as shocks and slip surfaces across zonal interfaces. Several example calculations including supersonic flow over a cylinder and blast-wave diffraction by a ramp demonstrate the robustness of the scheme and also the quality of the results that are possible with the zonal-boundary scheme.

0021-9991/86 $3.00

The zonal scheme as developed in Refs. [1] and [2] can be used with first-order-accurate, explicit integration schemes. However, first-order-accurate integration schemes are insufficient to produce accurate results for a general class of problems. In Ref. [3] the zonal scheme of Rai *et al.* and Rai [1, 2] is extended so that it can be used in conjunction with second-order-accurate, implicit, integration schemes such as the Beam–Warming scheme [4] and an implicit form of the Osher scheme [5]. Both these integration schemes use approximate factorization to retain the block-tridiagonal nature of the implicit equations in two- and three-spatial dimensions. The implicit zonal-boundary condition, however, is developed so that it can be used with both factored and unfactored schemes.

The use of implicit integration schemes in conjunction with an implicit zonal-boundary scheme results in increasing the convergence rate by more than an order of magnitude (when compared to the explicit calculations) in the inviscid demonstration calculations of Ref. [3]. The importance of implicit zonal schemes for viscous calculations can hardly be overemphasized. The fine grids required to resolve boundary layer properties result in extremely restrictive time-step limitations for explicit schemes and make viscous calculations with explicit schemes impractical. To efficiently perform implicit, viscous calculations on patched grids, it is important to treat the zonal-boundary points implicitly as well.

The factored implicit integration schemes used in Ref. [3] have the following disadvantages:

(1) The convergence speed (for problems with asymptotic steady states) reaches a maximum at a rather small step-size value instead of increasing continually with increasing step size.

(2) Factored, implicit integration schemes are more difficult to program in a zonal setting when compared to relaxation schemes.

Chakravarthy [6] presents a relaxation approach to solving the Euler equations. Both time-accurate and steady-state results can be obtained with this technique. The relaxation approach can be used with a certain class of upwind schemes. Relaxation is possible because of the desirable properties of this class of schemes; in particular, the total variation diminishing (TVD) property. The TVD property provides us with the diagonal dominance that is required to perform stable calculations with the relaxation approach (for large time steps). Typically, relaxation schemes do not have the disadvantages of factored schemes mentioned above. Further details of the relaxation approach can be found in Ref. [6].

In this study we investigate the possibility of using the relaxation approach in a zonal setting where several grids are patched together to discretize the region of interest. The relaxation approach has the advantage that it results in a simpler formulation of the implicit, zonal-boundary condition than that necessary for factored integration schemes. However, it should be remembered that the integration scheme has to be TVD for relaxation to work. The implicit, factored zonal approach [3] is the preferred technique when the integration scheme is not TVD. The equations

necessary to merge the zonal and relaxation approaches are presented in the following section. Demonstration calculations including supersonic flow over a cylinder and the motion of a Lamb-type vortex through a zonal boundary are presented. The cylinder calculation demonstrates the increase in convergence rate and the consequent decrease in computing costs (when compared to an explicit scheme) that are possible with the relaxation approach. The vortex calculation demonstrates the time-accuracy and quality of solutions possible with the implicit, zonal-relaxation scheme.

One of the most important applications of the zonal approach is the treatment of flow regions that are associated with bodies which have some parts that move relative to others; for example, the helicopter rotor–fuselage combination or the rotor–stator configurations found in turbines and compressors. It is impractical to have a single grid that envelopes both the moving and stationary parts of the system. This problem can be overcome simply by containing the stationary parts in one zone (or set of zones) and the moving parts in another zone (or set of zones). The zones that contain the moving parts can be made to be stationary relative to the moving parts. This approach gives rise to zonal boundaries (where the moving and stationary zones meet) at which one set of grid points move relative to others. The zonal-boundary treatment in this case has to be time-accurate (in addition to the usual requirement of spatial accuracy) to yield reasonable results. The time-accuracy that is possible in such zonal calculations has already been demonstrated in [3]. In this study an application of this technology is presented. The application consists of two parabolic-arc airfoils that move relative to each other similar to the airfoils in a rotor–stator combination. Results in the form of surface pressure histories and time-varying pressure contours are included.

The Integration Scheme

The implicit, relaxation-zonal scheme is developed within the framework of an iterative, implicit relaxation scheme [6]. In Ref. [6], the relaxation technique is developed in a very general manner so that it can be used with several upwind schemes. In this study, a particular form that can be used with the first- and second-order accurate Osher schemes is presented. Although the flux linearizations that are required for the technique are developed with the Osher scheme in mind, they can be used equally effectively with the split-flux scheme [7] and with Roe's scheme [8].

To develop the finite-difference equations for the relaxation technique we consider the unsteady Euler equations in two dimensions

$$Q_t + E_x + F_y = 0. \tag{1}$$

The vectors Q, E, and F are given by

$$Q=\begin{bmatrix}\rho\\ \rho u\\ \rho v\\ e\end{bmatrix},\qquad E=\begin{bmatrix}\rho u\\ p+\rho u^2\\ \rho uv\\ (e+p)\,u\end{bmatrix},\qquad F=\begin{bmatrix}\rho v\\ \rho uv\\ p+\rho v^2\\ (e+p)\,v\end{bmatrix}, \tag{2}$$

where ρ is the density, p is the pressure, u and v are velocities in the x and y directions, respectively, and e is the total internal energy per unit volume

$$e=\frac{p}{\gamma-1}+\frac{\rho}{2}\,(u^2+v^2). \tag{3}$$

Establishing the independent variable transformation

$$\begin{aligned}\tau&=t,\\ \xi&=\xi(x,y,t),\\ \eta&=\eta(x,y,t),\end{aligned} \tag{4}$$

and applying this transformation to Eq. (1), the following is obtained:

$$\tilde{Q}_\tau+\tilde{E}_\xi+\tilde{F}_\eta=0, \tag{5}$$

where

$$\begin{aligned}\tilde{Q}&=Q/J,\\ \tilde{E}(Q,\xi)&=[\xi_t Q+\xi_x E+\xi_y F]/J,\\ \tilde{F}(Q,\eta)&=[\eta_t Q+\eta_x E+\eta_y F]/J,\\ J&=\xi_x\eta_y-\eta_x\xi_y.\end{aligned} \tag{6}$$

The notation $\tilde{E}(Q,\xi)$ and $\tilde{F}(Q,\eta)$ is used to show the dependence of these quantities on the metrics of the transformation.

A fully implicit conservative finite-difference scheme for Eq. (5) can be written as

$$\frac{\tilde{Q}_{j,k}^{n+1}-\tilde{Q}_{j,k}^{n}}{\Delta\tau}+\frac{\hat{E}_{j+1/2,k}^{n+1}-\hat{E}_{j-1/2,k}^{n+1}}{\Delta\xi}+\frac{\hat{F}_{j,k+1/2}^{n+1}-\hat{F}_{j,k-1/2}^{n+1}}{\Delta\eta}=0, \tag{7}$$

where $\hat{E}_{j+1/2,k}$ and $\hat{F}_{j,k+1/2}$ are numerical fluxes that are consistent with the transformed physical fluxes $\tilde{E}$ and $\tilde{F}$. Equation (7) represents a fully implicit scheme since the fluxes are evaluated at the $(n+1)$th time-level. Evaluation of these fluxes at the $(n+1)$th time-level results in a system of nonlinear equations that need to be solved in an iterative manner. The usual strategy that is imployed at this stage is the linearization of the numerical fluxes with respect to the time-like variable τ. The resulting system of linear equations is then solved in order to update the dependent

variables. Since the terms that appear in the linearization process depend on the scheme used to evaluate the numerical fluxes, we now confine the development to the schemes used in this study, that is, the first- and second-order Osher schemes.

The First-Order-Accurate Osher Scheme

The numerical flux for the first-order-accurate Osher scheme is given by Ref. [9],

$$\hat{E}^{n+1}_{j+1/2,k} = \tfrac{1}{2}[\tilde{E}(Q_{j,k}, \xi_{j+1/2,k}) + \tilde{E}(Q_{j+1,k}, \xi_{j+1/2,k}) - \Delta E^{+}(Q_{j,k}, Q_{j+1,k}, \xi_{j+1/2,k}) + \Delta E^{-}(Q_{j,k}, Q_{j+1,k}, \xi_{j+1/2,k})]^{n+1}, \quad (8)$$

where

$$[\Delta E^{\pm}(Q_{j,k}, Q_{j+1,k}, \xi_{j+1/2,k})]^{n+1} = \int_{Q^{n+1}_{j,k}}^{Q^{n+1}_{j+1,k}} \left[\frac{\partial \tilde{E}}{\partial Q}(Q, \xi_{j+1/2,k})\right]^{\pm} dQ. \quad (9)$$

The numerical flux $\hat{F}^{n+1}_{j,k+1/2}$ can be obtained in a similar manner. The evaluation of the integral in Eq. (9) can be found in Ref. [9].

The time-linearization of the numerical flux $\hat{E}^{n+1}_{j+1/2,k}$ requires the linearization of the integral given in Eq. (9). The linearization of this integral is a cumbersome process that is computationally expensive. Hence, the following approximation [5] is made to simplify the linearization process:

$$\left[\frac{\partial \tilde{E}}{\partial Q}(Q, \xi_{j+1/2,k})\right]^{\pm} \cong \frac{\partial}{\partial Q}[\tilde{E}^{\pm}(Q, \xi_{j+1/2,k})], \quad (10)$$

where

$$\tilde{E}^{\pm}(Q, \xi_{j+1/2,k}) = \left[\frac{\partial \tilde{E}}{\partial Q}(Q, \xi_{j+1/2,k})\right]^{\pm} Q. \quad (11)$$

Substituting Eq. (10) into Eq. (9) yields

$$[\Delta E^{\pm}(Q_{j,k}, Q_{j+1,k}, \xi_{j+1/2,k})]^{n+1} = (\tilde{E}^{\pm}_{j+1,k} - \tilde{E}^{\pm}_{j,k})^{n+1}. \quad (12)$$

Equations (8) and (12) together yield

$$(\hat{E}^{n+1}_{j+1/2,k})_{\text{approx}} = [\tilde{E}^{+}(Q_{j,k}, \xi_{j+1/2,k}) + \tilde{E}^{-}(Q_{j+1,k}, \xi_{j+1/2,k})]^{n+1}. \quad (13)$$

Linearizing Eq. (13) with respect to τ and making use of Eq. (10) once again, it can be shown that

$$(\hat{E}^{n+1}_{j+1/2,k})_{\text{approx}} = (\hat{E}^{n}_{j+1/2,k})_{\text{approx}} + (\tilde{A}^{+}_{j,k})^{n} \Delta \tilde{Q}_{j,k} + (\tilde{A}^{-}_{j+1,k})^{n} \Delta \tilde{Q}_{j+1,k}, \quad (14)$$

where

$$\tilde{A}^{\pm}_{j,k} = \left[\frac{\partial \tilde{E}}{\partial \tilde{Q}}\,(Q_{j,k}, \xi_{j+1/2,k})\right]^{\pm}. \tag{15}$$

The numerical flux for the first-order-accurate Osher scheme using this approximate linearization can now be written as

$$\hat{E}^{n+1}_{j+1/2,k}(\text{linearized}) = \hat{E}^{n}_{j+1/2,k} + [\tilde{A}^{+}(Q_{j,k}, \xi_{j+1/2,k})\,\Delta\tilde{Q}_{j,k} + \tilde{A}^{-}(Q_{j+1,k}, \xi_{j+1/2,k})\,\Delta\tilde{Q}_{j+1,k}]^{n}, \tag{16}$$

where $\hat{E}^{n}_{j+1/2,k}$ is as defined in Eq. (8) (except that the time-level at which it is evaluated is n and not $(n+1)$). It should be noted that the use of the approximate linearization does not result in any loss of the conservative properties of the scheme.

The iterative implicit technique of Ref. [6] as applied to the first-order-accurate Osher scheme now takes the form

$$\left[I + \frac{\Delta\tau}{\Delta\xi}[\nabla_{\xi}\tilde{A}^{+}_{j,k} + \Delta_{\xi}\tilde{A}^{-}_{j,k}] + \frac{\Delta\tau}{\Delta\eta}[\nabla_{\eta}\tilde{B}^{+}_{j,k} + \Delta_{\eta}\tilde{B}^{-}_{j,k}]\right]^{p}[\tilde{Q}^{p+1}_{j,k} - \tilde{Q}^{p}_{j,k}] = -\Delta\tau\left[\frac{\tilde{Q}^{p}_{j,k} - \tilde{Q}^{n}_{j,k}}{\Delta\tau} + \frac{\hat{E}^{p}_{j+1/2,k} - \hat{E}^{p}_{j-1/2,k}}{\Delta\xi} + \frac{\hat{F}^{p}_{j,k+1/2} - \hat{F}^{p}_{j,k-1/2}}{\Delta\eta}\right], \tag{17}$$

where $\tilde{Q}^{p}$ is an approximation to Q^{n+1} and Δ and ∇ are forward and backward difference operators, respectively. When $p=0$, $\tilde{Q}^{p}=\tilde{Q}^{n}$, and when Eq. (17) is iterated to convergence at a given time-step, $\tilde{Q}^{p}=\tilde{Q}^{n+1}$. It should be noted that, because the left-hand side of this equation can be made equal to zero at each time-step (by iterating to convergence), linearization errors can be driven to zero during the iterative process. For problems where only the asymptotic steady-state is of interest, the iteration process need not be carried to convergence at each time-step. In fact, when the number of iterations is restricted to one, the scheme reverts to a conventional, noniterative scheme [4] (but unfactored).

Unfortunately, Eq. (17) is extremely time-consuming to solve in a direct fashion because of the large bandwidth of the matrix on the left-hand side. Whereas factorization reduces the bandwidth of this matrix (the single matrix is converted into two tridiagonal matrices), it introduces a new set of problems. It is at this point that relaxation schemes can be used efficiently to solve Eq. (17). The iterative form of Eq. (17) is ideally suited to relaxation schemes. Although there are a host of different relaxation schemes available, the ones that have been chosen for this study are the point-wise and line-relaxation schemes of the non-Gauss–Seidel type. The point-wise relaxation scheme is obtained by discarding all the nondiagonal terms on the left-hand side of Eq. (17). This yields

$$\left[I + \Delta\tau\left(\frac{\tilde{A}^{+}_{j,k} - \tilde{A}^{-}_{j,k}}{\Delta\xi} + \frac{\tilde{B}^{+}_{j,k} - \tilde{B}^{-}_{j,k}}{\Delta\eta}\right)\right]^{p}(\tilde{Q}^{p+1}_{j,k} - \tilde{Q}^{p}_{j,k}) = \text{r.h.s. of Eq. (17)}. \tag{18}$$

The line-relaxation scheme is obtained by retaining all the diagonal terms and all the terms that correspond to points on a given line, for example, a constant η-line. This yields

$$\left[I+\frac{\Delta\tau}{\Delta\xi}(\nabla_\xi \tilde{A}^+_{j,k}+\Delta_\xi \tilde{A}^-_{j,k})+\frac{\Delta\tau}{\Delta\eta}(\tilde{B}^+_{j,k}-\tilde{B}^-_{j,k})\right]^p(\tilde{Q}^{p+1}_{j,k}-\tilde{Q}^p_{j,k})=\text{r.h.s. of Eq. (17)} \quad (19)$$

If the constant ξ-lines had been chosen instead, the resulting equations would be

$$\left[I+\frac{\Delta\tau}{\Delta\xi}(\tilde{A}^+_{j,k}-\tilde{A}^-_{j,k})+\frac{\Delta\tau}{\Delta\eta}(\nabla_\eta \tilde{B}^+_{j,k}+\Delta_\eta \tilde{B}^-_{j,k})\right]^p(\tilde{Q}^{p+1}_{j,k}-\tilde{Q}^p_{j,k})=\text{r.h.s. of Eq. (17)} \quad (20)$$

Variants of the line and point-wise relaxation schemes such as the zebra and checkerboard schemes are also discussed in Ref. [6].

Although Eq. (17) is fully conservative (in spite of the approximate linearization), Eqs. (18)–(20) are not conservative in time unless they are iterated to convergence at each time-step (this would be necessary for time-dependent problems where the transients are of interest). However, for problems where only the time-asymptotic solutions are required, Eqs. (18)–(20) yield solutions that satisfy the conservation laws at steady-state without requiring iteration-to-convergence at each time-step. This is because the right-hand side of these equations is fully conservative.

The Second-Order-Accurate Osher Scheme

The numerical flux for the fully implicit second-order-accurate Osher scheme is given by Ref. [9],

$$\bar{E}^{n+1}_{j+1/2,k}=\hat{E}^{n+1}_{j+1/2,k}[\text{first-order Osher scheme}]+\tfrac{1}{2}[\Delta E^+(Q_{j-1,k}, Q_{j,k}, \xi_{j+1/2,k}) - \Delta E^-(Q_{j+1,k}, Q_{j+2,k}, \xi_{j+1/2,k})]^{n+1}, \quad (21)$$

where $\Delta E^\pm$ are evaluated as before. Note that the numerical flux for the second-order scheme is denoted by $\bar{E}^{n+1}_{j+1/2,k}$ to distinguish it from the numerical flux for the first-order Osher scheme. Linearization of all the terms in Eq. (21) would result in block-pentadiagonal matrices for line-relaxation schemes. Hence, only the terms corresponding to the first-order scheme and those second-order terms that contribute to the diagonal elements of the matrix are linearized (private communication, S. R. Chakravarthy, Rockwell International Science Center). The resulting iterative, implicit scheme takes the form

$$\left[I+\frac{\Delta\tau}{\Delta\xi}\left[\frac{1}{2}(\tilde{A}^{+}_{j,k}-\tilde{A}^{-}_{j,k})+\nabla_{\xi}\tilde{A}^{+}_{j,k}+\Delta_{\xi}\tilde{A}^{-}_{j,k}\right]\right.$$
$$\left.+\frac{\Delta\tau}{\Delta\eta}\left[\frac{1}{2}(\tilde{B}^{+}_{j,k}-\tilde{B}^{-}_{j,k})+\nabla_{\eta}\tilde{B}^{+}_{j,k}+\Delta_{\eta}\tilde{B}^{-}_{j,k}\right]\right]^{p}(\tilde{Q}^{p+1}_{j,k}-\tilde{Q}^{p}_{j,k})$$
$$=-\Delta\tau\left[\frac{\tilde{Q}^{p}_{j,k}-\tilde{Q}^{n}_{j,k}}{\Delta\tau}+\frac{\hat{E}^{p}_{j+1/2,k}-\hat{E}^{p}_{j-1/2,k}}{\Delta\xi}+\frac{\hat{F}^{p}_{j,k+1/2}-\hat{F}^{p}_{j,k-1/2}}{\Delta\eta}\right]$$
$$-\frac{\Delta\tau}{2\,\Delta\xi}\left[\overline{\Delta E}^{+}(Q_{j-1,k},Q_{j,k},\xi_{j+1/2,k})-\overline{\Delta E}^{+}(Q_{j-2,k},Q_{j-1,k},\xi_{j-1/2,k})\right]^{p}$$
$$+\frac{\Delta\tau}{2\,\Delta\xi}\left[\overline{\Delta E}^{-}(Q_{j+1,k},Q_{j+2,k},\xi_{j+1/2,k})-\overline{\Delta E}^{-}(Q_{j,k},Q_{j+1,k},\xi_{j-1/2,k})\right]^{p}$$
$$-\frac{\Delta\tau}{2\,\Delta\eta}\left[\overline{\Delta F}^{+}(Q_{j,k-1},Q_{j,k},\eta_{j,k+1/2})-\overline{\Delta F}^{+}(Q_{j,k-2},Q_{j,k-1},\eta_{j,k-1/2})\right]^{p}$$
$$+\frac{\Delta\tau}{2\,\Delta\eta}\left[\overline{\Delta F}^{-}(Q_{j,k+1},Q_{j,k+2},\eta_{j,k+1/2})-\overline{\Delta F}^{-}(Q_{j,k},Q_{j,k+1},\eta_{j,k-1/2})\right]^{p}. \quad (22)$$

The terms that result in second-order spatial accuracy [on the right-hand side of Eq. (22)] have been modified, that is, these flux differences are obtained from a flux-limiting process [9]. Flux-limiting is essential to provide the diagonal dominance required for relaxation schemes [6]. The linearization of the second-order terms is carried out before the flux limiting process is performed.

The point-wise relaxation scheme is now obtained by discarding all nondiagonal terms, that is,

$$\left[I+\frac{1.5\,\Delta\tau}{\Delta\xi}(\tilde{A}^{+}_{j,k}-\tilde{A}^{-}_{j,k})+\frac{1.5\,\Delta\tau}{\Delta\eta}(\tilde{B}^{+}_{j,k}-\tilde{B}^{-}_{j,k})\right]^{p}(\tilde{Q}^{p+1}_{j,k}-\tilde{Q}^{p}_{j,k})$$
$$=\text{r.h.s. of Eq. (22)} \quad (23)$$

and the line-relaxation scheme corresponding to Eq. (19) takes the form

$$\left[I+\frac{1.5\,\Delta\tau}{\Delta\eta}(\tilde{B}^{+}_{j,k}-\tilde{B}^{-}_{j,k})+\frac{0.5\,\Delta\tau}{\Delta\xi}(\tilde{A}^{+}_{j,k}-\tilde{A}^{-}_{j,k})+\frac{\Delta\tau}{\Delta\xi}(\nabla_{\xi}\tilde{A}^{+}_{j,k}+\Delta_{\xi}\tilde{A}^{-}_{j,k})\right]^{p}$$
$$\times(\tilde{Q}^{p+1}_{j,k}-\tilde{Q}^{p}_{j,k})=\text{r.h.s. of Eq. (22).} \quad (24)$$

The comments regarding the conservative properties of the first-order schemes apply to the second-order schemes as well. As stated earlier, although Eqs. (17)–(24) have been developed for the Osher scheme, they are equally applicable to the split-flux scheme and Roe's scheme; only the evaluation of the fluxes on the right-hand side of these equations change according to the particular integration scheme that is chosen.

THE ZONAL-BOUNDARY SCHEME

The implicit, zonal-boundary condition is similar to its explicit counterpart insofar as the computation of the numerical fluxes (which appear on the right-hand side of Eq. (17)) in the vicinity of zonal boundaries is concerned. Hence, in this section the explicit, zonal-boundary scheme [2] is first outlined, followed by a presentation of the necessary extensions to this scheme to make it compatible with implicit relaxation techniques.

Review of the Explicit Zonal Scheme

Consider the two curvilinear grids used to discretize the flow region shown in Fig. 1. The line AB represents the zonal boundary that separates the two grids used to discretize the given region. Let l and m be the indices used in the ξ- and η-directions, respectively, in zone 1, and let j and k be the corresponding indices for zone 2. The notation used in this study is different from that used in Ref. [2] (m and k increase in opposite directions in [2]). Let n represent the time-step for both zones. A superscript within parentheses will denote the zone to which a given quantity belongs, for example, $\Delta\tau^{(1)}$ denotes the marching step-size in zone 1.

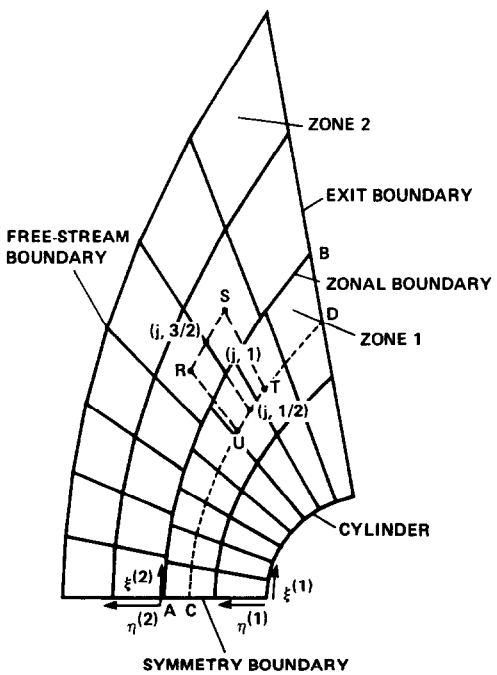

FIG. 1. Two-zone grid to illustrate the zonal scheme in curvilinear coordinates.

Establishing two independent variable transformations (one for each grid)

$$\begin{aligned} \tau^{(i)} &= t, \\ \xi^{(i)} &= \xi^{(i)}(x, y, t), \qquad i = \begin{cases} 1 & \text{for zone 1} \\ 2 & \text{for zone 2} \end{cases} \\ \eta^{(i)} &= \eta^{(i)}(x, y, t), \end{aligned} \tag{25}$$

and applying these transformations to Eq. (1), the following equation is obtained

$$\tilde{Q}^{(i)}_{\tau^{(i)}} + \tilde{E}^{(i)}_{\xi^{(i)}} + \tilde{F}^{(i)}_{\eta^{(i)}} = 0, \qquad i = 1, 2, \tag{26}$$

where

$$\begin{aligned} \tilde{Q}^{(i)} &= Q/J^{(i)}, \\ \tilde{E}^{(i)}[Q, \xi^{(i)}] &= [\xi^{(i)}_t Q + \xi^{(i)}_x E + \xi^{(i)}_y F]/J^{(i)}, \\ \tilde{F}^{(i)}[Q, \eta^{(i)}] &= [\eta^{(i)}_t Q + \eta^{(i)}_x E + \eta^{(i)}_y F]/J^{(i)}, \\ J^{(i)} &= \xi^{(i)}_x \eta^{(i)}_y - \eta^{(i)}_x \xi^{(i)}_y. \end{aligned} \tag{27}$$

Let the conservative difference schemes used to integrate Eq. (26) be given by

$$\frac{\Delta \tilde{Q}^{(1)}_{l,m}}{\Delta \tau^{(1)}} + \frac{\hat{E}^{(1)}_{l+1/2,m} - \hat{E}^{(1)}_{l-1/2,m}}{\Delta \xi^{(1)}} + \frac{\hat{F}^{(1)}_{l,m+1/2} - \hat{F}^{(1)}_{l,m-1/2}}{\Delta \eta^{(1)}} = 0 \tag{28}$$

and

$$\frac{\Delta \tilde{Q}^{(2)}_{j,k}}{\Delta \tau^{(2)}} + \frac{\hat{E}^{(2)}_{j+1/2,k} - \hat{E}^{(2)}_{j-1/2,k}}{\Delta \xi^{(2)}} + \frac{\hat{F}^{(2)}_{j,k+1/2} - \hat{F}^{(2)}_{j,k-1/2}}{\Delta \eta^{(2)}} = 0, \tag{29}$$

where $\hat{E}^{(i)}$ and $\hat{F}^{(i)}$ are once again numerical fluxes consistent with the transformed fluxes $\tilde{E}$ and $\tilde{F}$. For the explicit integration scheme these numerical fluxes are evaluated at the nth time-level.

The explicit zonal scheme consists of the following three steps:

(1) Integration of the dependent variables at grid points (of both the grids) that do not belong to the zonal boundary using Eqs. (28) and (29).

(2) Integration of the dependent variables at the zonal-boundary points of one of the zones (e.g., zone 2 of Fig. 1) using a scheme that conserves fluxes across the zonal boundary.

(3) Calculation of the dependent variables at the zonal-boundary points of the other zone (e.g., zone 1 of Fig. 1) such that the dependent variables are continuous across the zonal boundary.

The implementation of the first step of the zonal scheme is straightforward. The implementation of the second step is described below. Assume that the zonal-boundary points of zone 2 are to be updated using the finite-difference scheme of

Eq. (29). This calculation requires the use of the fluxes $\hat{F}^{(2)}_{j,1/2}$. These fluxes have to be calculated so that global conservation is maintained. A typical cell (points *RSTU*) of a zonal-boundary point $(j, 1)$ is shown in Fig. 1. The points R and S are midpoints of the cells in which they reside whereas the points T and U are obtained as follows: The constant j-lines of zone 2 are extrapolated into zone 1 to intersect the line CD (CD corresponds to $m = m\max - \frac{1}{2}$ in zone 1 and to $k = \frac{1}{2}$ in zone 2). The intersection points have the indices $(j, \frac{1}{2})$. Point T is midway between the points $(j+1, \frac{1}{2})$ and $(j, \frac{1}{2})$ and point U is midway between points $(j, \frac{1}{2})$ and $(j-1, \frac{1}{2})$. The global conservation property can be shown to be satisfied if the following relationship is satisfied

$$\tfrac{1}{2}[\hat{F}^{(2)}_{1,1/2} + \hat{F}^{(2)}_{j\max,1/2}] + \sum_{j=2}^{j\max-1} \hat{F}^{(2)}_{j,1/2}$$

$$= \tfrac{1}{2}[\hat{F}^{(1)}_{1,m\max-1/2} + \hat{F}^{(1)}_{l\max,m\max-1/2}] + \sum_{l=2}^{l\max-1} \hat{F}^{(1)}_{l,m\max-1/2}. \tag{30}$$

A close examination of Eq. (30) shows that each side of this equation is nothing but a discrete form of the line integral of the numerical flux $\hat{F}$ along the line CD in Fig. 1 whereas the equation itself represents flux conservation across the zonal boundary. Equation (30) is only a necessary condition and is not sufficient to define the fluxes $\hat{F}^{(2)}_{j,1/2}$ in a physically meaningful way.

Assume that the $\hat{F}^{(2)}_{j,1/2}$ are obtained by interpolating the $\hat{F}^{(1)}_{l,m\max-1/2}$, that is,

$$\hat{F}^{(2)}_{j,1/2} = \sum_{l=p}^{q} N_{j,l} \hat{F}^{(1)}_{l,m\max-1/2}, \tag{31}$$

where the $N_{j,l}$ are interpolation coefficients and p and q define the set of fluxes of zone 1 that will be used in the interpolation. We now describe a simple way of obtaining the interpolation coefficients $N_{j,l}$ such that Eq. (30) is automatically satisfied. Let the line CD in Fig. 2 correspond to the line CD in Fig. 1. The dots represent the grid points of zone 1 and the crosses represent those of zone 2. A running parameter s is established along the line CD. The quantity s represents the distance of a point from the point C along the curve CD. Representative numerical values of $\hat{F}^{(1)}_{l,m\max-1/2}$ are plotted on the positive y axis. Assume a piece-wise constant variation of the numerical fluxes $\hat{F}^{(1)}_{l,m\max-1/2}$ along CD, that is, $\hat{F}^{(1)}_{l,m\max-1/2}$ is costant between $s^{(1)}_{l-1/2}$ and $s^{(1)}_{l+1/2}$. Consider a point of zone 2, $(j, 1)$. The $\hat{F}^{(2)}_{j,1/2}$ is now calculated from

$$\hat{F}^{(2)}_{j,1/2}(Q, \eta^{(2)}_{j,1/2}) = \int_U^T \frac{\hat{F}^{(1)}_{l,m\max-1/2}(Q, \eta^{(1)}_{l,m\max-1/2})\, ds}{(s^{(1)}_{l+1/2} - s^{(1)}_{l-1/2})}$$

$$= \sum_{l=p}^{q} N_{j,l} \hat{F}^{(1)}_{l,m\max-1/2}, \tag{32}$$

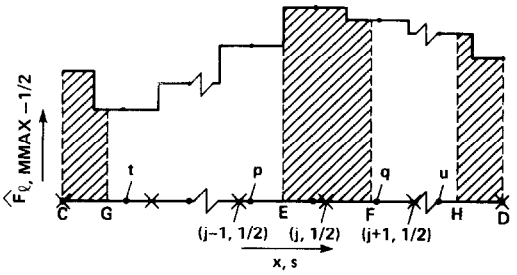

FIG. 2. Piece-wise constant variation of the numerical flux $\hat{F}$ as a function of s.

where the values of $N_{j,l}$ are given by

$$N_{j,l} = \begin{cases} 0 & \text{if } s^{(1)}_{l+1/2},\, s^{(1)}_{l-1/2} \leqslant s^{(2)}_{j-1/2} \\ 0 & \text{if } s^{(1)}_{l+1/2},\, s^{(1)}_{l-1/2} \geqslant s^{(2)}_{j+1/2} \\ \dfrac{[\min(s^{(2)}_{j+1/2},\, s^{(1)}_{l+1/2}) - \max(s^{(2)}_{j-1/2},\, s^{(1)}_{l-1/2})]}{s^{(1)}_{l+1/2} - s^{(1)}_{l-1/2}}. \end{cases} \tag{33}$$

The simple expressions of Eq. (33) are valid only for a piece-wise constant variation of the $\hat{F}^{(1)}_{l,m\max-1/2}$. A piece-wise linear or any other variation would result in different formulae for the interpolation coefficients $N_{j,l}$. Equation (33), in an indirect manner, also yields the endpoints in the interpolation, p and q (p and q include only that set of fluxes of zone 1 that are multiplied by a nonzero interpolation coefficient for the given flux of zone 2). The treatment of the points (1, 1) and ($j$max, 1) and the calculation of the metrics used in the integration of the zonal points can be found in Ref. [2].

The final step of the zonal scheme consists of updating the zonal-boundary points of zone 1 so that the dependent variables are continuous across the zonal boundary. This is very simply done by an interpolation process. The dependent variables at the zonal-boundary points of zone 1 are obtained by interpolating the updated dependent variables at the zonal-boundary points of zone 2. The linear interpolation of the dependent variables and the line integration of the piece-wise constant fluxes results in first-order accuracy at the zonal boundary. Higher order interpolations are currently being investigated.

The foregoing discussion assumed that the numerical fluxes $\hat{F}^{(1)}_{l,m\max-1/2}$ were readily available. For the first-order-accurate Osher scheme an examination of Eq. (8) will show that only the quantities $Q_{l,m\max-1}$, $Q_{l,m\max}$ and, $\eta_{l,m\max-1/2}$ are sufficient to define $\hat{F}^{(1)}_{l,m\max-1/2}$. Since these quantities are easily available, calculation of $\hat{F}^{(1)}_{l,m\max-1/2}$ is a simpler matter. However, for the second-order-accurate Osher scheme, Eq. (21) shows that the flux difference

$$\Delta F^{-}(Q^{(1)}_{l,m\max}, Q^{(1)}_{l,m\max+1}, \eta^{(1)}_{l,m\max-1/2})$$

is required to calculate $\bar{F}^{(1)}_{l,m\max-1/2}$. The calculation of this flux difference, in turn,

requires the vector $Q^{(1)}_{l,m\max+1}$ (the line $m\max+1$ in zone 1 corresponds to the line $k=2$ in zone 2). The vector $Q^{(1)}_{l,m\max+1}$ is determined simply by extrapolating the constant-l lines into zone 2 to intersect the line $k=2$ in zone 2. The values of $Q^{(1)}_{l,m\max+1}$ are then interpolated from the values of $Q^{(2)}_{j,2}$. A simple linear interpolation was used to obtain the results presented in this paper. An alternative to this procedure that avoids the interpolation described above, is one which calculates the flux differences $\Delta F^-(Q^{(2)}_{j,1}, Q^{(2)}_{j,2}, \eta^{(2)}_{j,1/2})$ and which performs a flux balance as follows:

$$\Delta F^-(Q^{(1)}_{l,m\max}, Q^{(1)}_{l,m\max+1}, \eta^{(1)}_{l,m\max-1/2}) = \sum_{j=p}^{q} N_{l,j}\Delta F^-(Q^{(2)}_{j,1}, Q^{(2)}_{j,2}, \eta^{(2)}_{j,1/2}). \quad (34)$$

Note that in Eq. (34) the flux balance is being performed in the opposite direction (compared to the flux balance described earlier). Similar procedures, that is, interpolation or an additional flux balance, are required to calculate the numerical flux $\bar{F}^{(2)}_{j,3/2}$ also. Both methods, described above, do not in any way affect the conservative property of the zonal scheme. The additional flux difference terms that are required for the second-order-accurate integration scheme are once again perfectly balanced across the zonal boundary.

The Implicit, Relaxation-Zonal Scheme

Now that the calculation of the boundary fluxes has been described it remains to be shown how these ideas fit into the schemes as given by Eqs. (18)–(24). The right-hand side of all these equations can be calculated at all grid points in the interior and at the zonal boundary, using either the usual definition of numerical fluxes or by using the method described in the previous subsection.

The point-wise relaxation schemes given by Eqs. (18) and (23) remain completely unchanged except for the right-hand side at the zonal boundaries. This is because spatial derivatives of the matrices $\tilde{A}^{\pm}$ and $\tilde{B}^{\pm}$ do not appear on the left-hand side of these equations. For time-asymptotic problems the number of iterations per time-step can be restricted to just one. If for reasons of computational efficiency (increased convergence rates) it becomes necessary to use more than one iteration per time-step, then the most reasonable approach seems to be to perform each iteration in all the zones before performing the next iteration.

For the example shown in Fig. 1, where the constant ξ-lines are discontinuous at the zonal boundary, the line-relaxation schemes given by Eqs. (19) and (24) also remain unchanged as in the case of the point-wise relaxation schemes. This is because the η-derivatives of the matrices $\tilde{B}^+$ and $\tilde{B}^-$ do not appear on the left-hand side of these equations. However, the line relaxation scheme given by Eq. (20) needs to be modified at the zonal boundary of zone 2 because the backward difference $\nabla_\eta \tilde{B}^+_{j,k}$ is not defined. Several options are available to overcome this difficulty. The simplest solution would be to revert to the point-wise relaxation scheme at the zonal-boundary points, that is,

$$\left[I+\frac{\Delta\tau}{\Delta\xi}(\tilde{A}^{+}_{j,k}-\tilde{A}^{-}_{j,k})+\frac{\Delta\tau}{\Delta\eta}(\tilde{B}^{+}_{j,k}+\tilde{B}^{-}_{j,k})\right]^{p}(\tilde{Q}^{p+1}_{j,k}-\tilde{Q}^{p}_{j,k})=\text{r.h.s. of Eq. (17)} \quad (35)$$

when

$$k=1$$

and

$$\left[I+\frac{\Delta\tau}{\Delta\xi}(\tilde{A}^{+}_{j,k}-\tilde{A}^{-}_{j,k})+\frac{\Delta\tau}{\Delta\eta}(\nabla_\eta\tilde{B}^{+}_{j,k}+\Delta_\eta\tilde{B}^{-}_{j,k})\right]^{p}(\tilde{Q}^{p+1}_{j,k}-\tilde{Q}^{p}_{j,k})=\text{r.h.s. of Eq. (17)}$$

when

$$k\neq 1.$$

A second approach would be to retain only the diagonal terms from the derivative $\nabla_\eta\tilde{B}^{+}_{j,k}$ which then yields

$$\left[I+\frac{\Delta\tau}{\Delta\xi}(\tilde{A}^{+}_{j,k}-\tilde{A}^{-}_{j,k})+\frac{\Delta\tau}{\Delta\eta}(\tilde{B}^{+}_{j,k}+\Delta_\eta\tilde{B}^{-}_{j,k})\right]^{p}(\tilde{Q}^{p+1}_{j,k}-\tilde{Q}^{p}_{j,k})=\text{r.h.s. of Eq. (17)} \quad (36)$$

when

$$k=1$$

and

$$\left[I+\frac{\Delta\tau}{\Delta\xi}(\tilde{A}^{+}_{j,k}-\tilde{A}^{-}_{j,k})+\frac{\Delta\tau}{\Delta\eta}(\nabla_\eta\tilde{B}^{+}_{j,k}+\Delta_\eta\tilde{B}^{-}_{j,k})\right]^{p}(\tilde{Q}^{p+1}_{j,k}-\tilde{Q}^{p}_{j,k})=\text{r.h.s. of Eq. (17)}$$

when

$$k\neq 1.$$

The results presented in this study (and obtained with the line-relaxation schemes) were calculated using Eq. (36). The comments made earlier regarding the number of iterations per time-step (for the point-wise relaxation schemes) are valid for the line-relaxation schemes also.

The implicit, relaxation-zonal scheme can be summarized in the following steps:

(1) Integration of the dependent variables at all the grid points of zone 2 using the point-wise or the line-relaxation schemes with their special forms at the zonal-boundary (only one iteration).

(2) Interpolation of the newly obtained values of $[(Q^{(2)}_{j,1})^{p+1}-(Q^{(2)}_{j,1})^{p}]$ along the zonal boundary to obtain the values of $[(Q^{(1)}_{l,m\max})^{p+1}-(Q^{(1)}_{l,m\max})^{p}]$.

(3) Integration of the dependent variables at the grid points of zone 1 using the point-wise or line-relaxation schemes (only one iteration), and the most recent values of $[(\tilde{Q}^{(1)}_{l,m\max})^{p+1} - (\tilde{Q}^{(1)}_{l,m\max})^{p}]$ (a "Dirichlet-type" of boundary condition).

(4) Interpolation of the values of $(Q^{(2)}_{j,1})^{p+1}$ to obtain the values of $(Q^{(1)}_{l,m\max})^{p+1}$ (discard the ones obtained as a result of the integration).

(5) If the maximum value of the magnitudes of all $[(Q^{(i)})^{p+1} - (Q^{(i)})^{p}]$ is less than the prescribed tolerance limit, go to the next integration step; if not, go back to step 1 and reiterate.

Step 2 and the implementation of the Dirichlet boundary condition in step 3 are not required for point-wise relaxation schemes or for line-relaxation schemes where the lines are chosen so that they belong to the same family as the zonal-boundary line. It was found that for the approximately factored, implicit, zonal scheme [3] at least two iterations per time-step were required to perform stable calculations. In the case of implicit, relaxation-zonal schemes one iteration per time-step has been found to be sufficient to maintain stability. Multiple iterations are required only to obtain time-accuracy.

Results

Results are presented in this section for supersonic flow past a cylinder and the motion of a Lamb-type vortex through a zonal boundary. The unsteady Euler equations are integrated in time using relaxation schemes (point-wise relaxation and line relaxation) in conjunction with the new zonal-boundary conditions. Results are also presented for a model problem that simulates flow past a rotor–stator configuration. The results include time-dependent pressure contours and surface pressures.

Cylinder in a Supersonic Free Stream

The first test case consisted of a cylinder in supersonic flow. The free-stream Mach number that was chosen for this case was 2.0. The dependent variables at all grid points were initialized to their free-stream values. The finite-difference equations in addition to the various boundary conditions (including the zonal-boundary condition developed in this study) were integrated to convergence. The boundary condition used at the surface of the cylinder is implicit and characteristic in nature [6].

The grid used for the calculation is shown in Fig. 3. It consists of two zones patched together along the line AB. The discontinuity of the constant ξ-lines along the zonal boundary AB is clearly seen. The bow shock associated with this flow first appears at the surface of the cylinder and then moves outward through the zonal boundary to its converged position in zone 2.

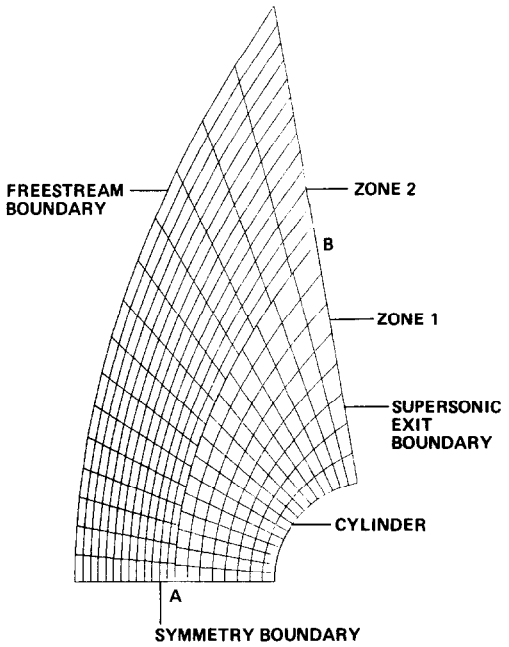

FIG. 3. Grid for the two-zone cylinder (supersonic) calculation.

The first calculation was performed with the first-order-accurate Osher scheme using a point-wise relaxation approach. Figure 4 shows the pressure contours obtained after 20 steps. Because of the large transients that occur during the first few steps of the calculation, the CFL number was initially restricted to 10.0. Table I gives the CFL numbers used at different stages of the calculation. The use of CFL numbers larger than 500.0 did not alter the convergence rate.

Figure 5 shows the pressure contours after 35 steps and Fig. 6 shows the contours after 60 steps. The smooth transition of the shock from zone 1 to zone 2 even at a zonal boundary in Figs. 6 and 7 demonstrates the quality of solutions possible with the present zonal scheme. The square symbols in Figs. 4–7 represent the converged shock position that is predicted by another numerical approach [10].

Figure 8 displays the convergence history for the first-order-explicit scheme and for the implicit relaxation scheme. The explicit scheme required approximately 2700 steps to converge. The convergence criterion chosen for this and the following cylinder calculations was

$$|\Delta\rho|_{\max} \leqslant 5 \times 10^{-4}$$

(based on a free-stream density value of 1.0). The relaxation scheme with only one

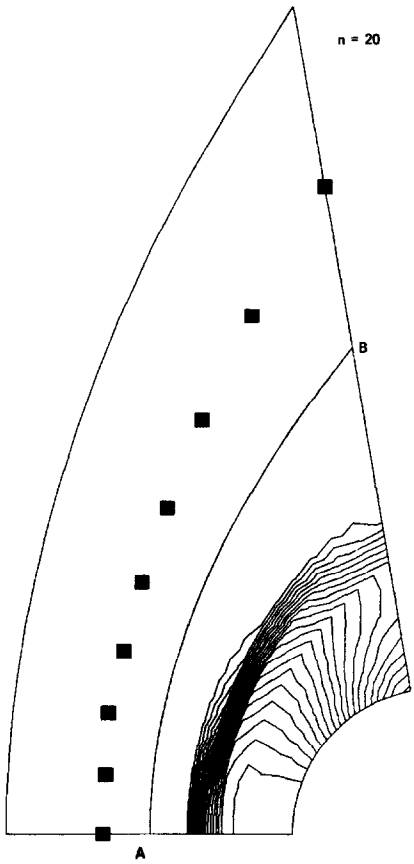

FIG. 4. Isobars after 20 integration steps (first-order Osher scheme).

iteration per step required 280 steps to converge, that is, the use of the implicit relaxation scheme increased the convergence rate by a factor of 9.65. Since the implicit scheme required 1.22 times as much computing time per step as the explicit scheme did, the actual computing cost was reduced by a factor of 7.91 with the use of the relaxation scheme. It should be remembered that the extra programming required to implement point-wise relaxation is minimal (typically, less than 100

TABLE I

Variation of CFL Number with Integration Step Number

Integration step (n)	CFL number
$0 < n \leqslant 10$	10.0
$10 < n$	500.0

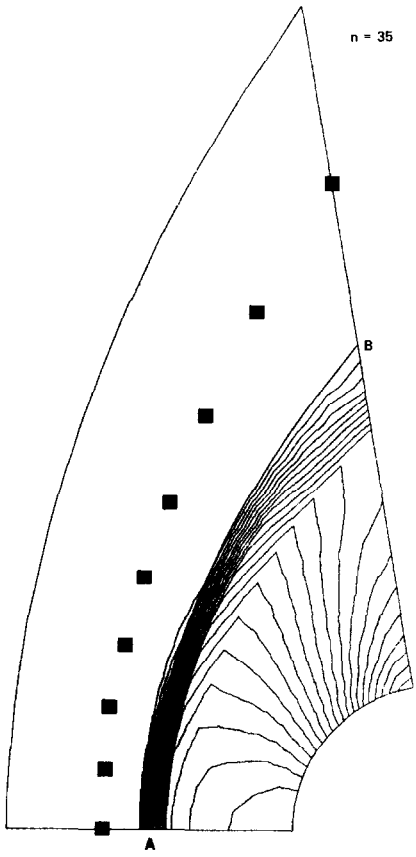

FIG. 5. Isobars after 35 integration steps (first-order Osher scheme).

lines of Fortran). Figure 8 also shows the convergence rate for the implicit relaxation scheme when two iterations are used at each time step. The scheme in this case required only 157 steps to converge. However, since it requires approximately twice as much computing time per step (compared to the relaxation scheme with one iteration per step) the total computing cost was almost the same. Figure 9 shows the variation of the magnitude of the maximum residue (R) in the continuity equation as a function of the number of integration steps

$$R = \left| \frac{\hat{E}^c_{j+1/2,k} - \hat{E}^c_{j-1/2,k}}{\Delta\xi} + \frac{\hat{F}^c_{j,k+1/2} - \hat{F}^c_{j,k-1/2}}{\Delta\eta} \right|_{\max},$$

where the superscript c represents the element of the vector corresponding to the continuity equation. The relaxation scheme with one iteration per step reduces R by 9 orders of magnitude in about 1000 steps and the scheme with two iterations per

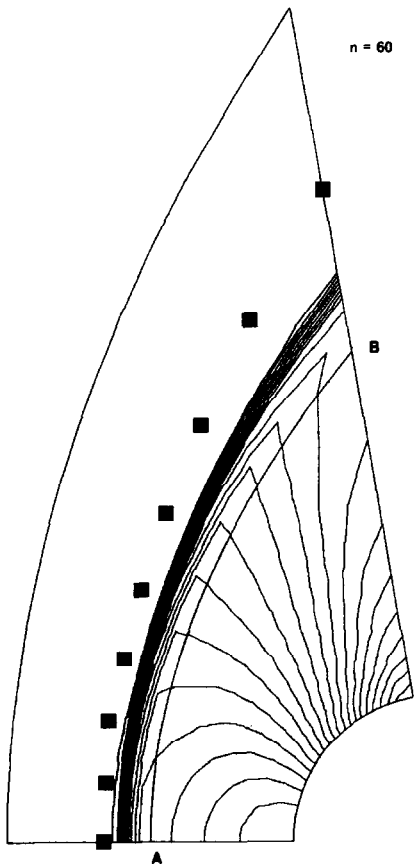

FIG. 6. Isobars after 60 integration steps (first-order Osher scheme).

step required about 500 steps to decrease R by the same amount. Table II summarizes the convergence rates and computing times for the variants of the first-order-accurate Osher scheme mentioned above. All computations were performed on a CRAY-XMP. The computer programs used in the present study were vectorized for use on this machine.

First-order-accurate schemes are insufficient to provide accurate results for a general class of problems. To obtain reliable results it is necessary to resort to second-order-accurate integration schemes. The first-order results presented in this study were included merely to demonstrate the increase in convergence rate (when compared to that obtained with the explicit zonal scheme [2]).

Figure 10 shows the pressure contours obtained at convergence with the implicit, second-order-accurate Osher scheme for the cylinder problem. This scheme uses flux limiters to achieve the TVD property in each spatial dimension. The shock position is predicted more accurately than in the previous case. The contours once

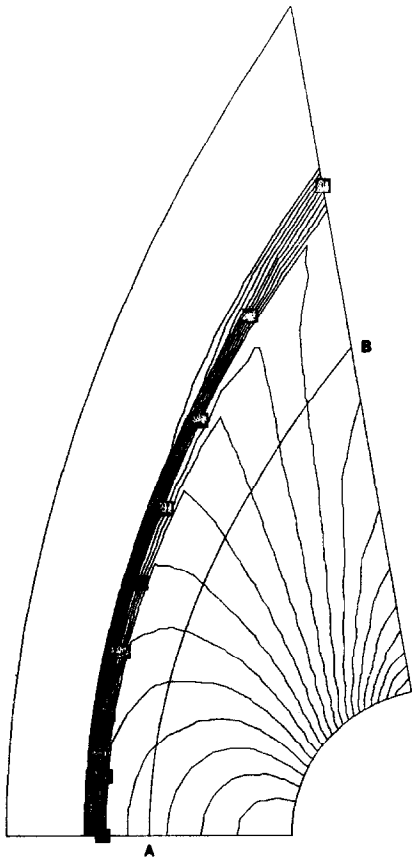

FIG. 7. Isobars at convergence (first-order Osher scheme).

again transition smoothly across the zonal boundary despite the discontinuity of the grid lines.

Figure 11 shows the convergence rates obtained with the implicit relaxation approach. A point-wise relaxation scheme was used for this set of calculations. The CFL number was varied as in the previous case. The explicit second-order-accurate TVD scheme required approximately 3000 steps to converge at a CFL number of 0.7. This translates into 97 sec of computing time (3.23 sec/100 steps) to obtain the converged solution. At a CFL number of 500 and with one iteration per time-step, the relaxation scheme converged in 485 steps. Since this variant of the relaxation scheme requires 1.17 times as much computing time per time-step as the explicit scheme does, the computing cost was reduced by a factor of 5.30 with the use of the relaxation scheme. Figure 11 also shows the convergence history for a point-wise relaxation scheme with two iterations per time-step. This scheme required 255 steps to converge. However, the computing time required to obtain the converged

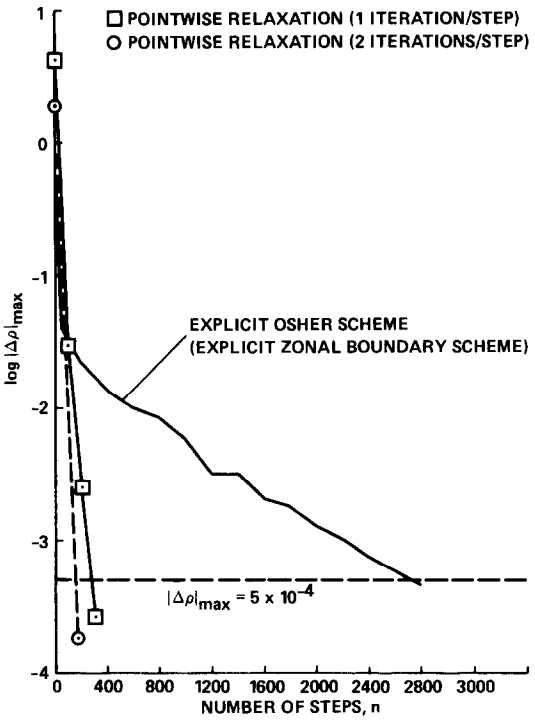

FIG. 8. Convergence history for the cylinder calculation (implicit point-wise relaxation and explicit first-order Osher-scheme calculations).

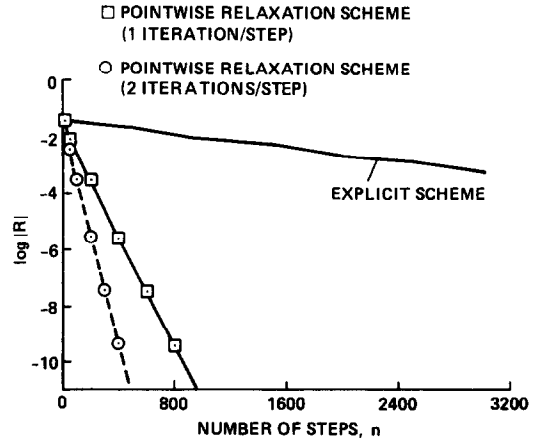

FIG. 9. Time history of the maximum residual in the continuity equation (first-order Osher scheme).

TABLE II

Computing Times for the First-Order Accurate Osher Scheme

Type of Osher scheme used	Explicit	Implicit Relaxation	
		1 iteration/step	2 iterations/step
Time per 100 steps, sec	2.46	3.00	5.88
Number of steps to converge	2700	280	157
Time to converge, sec	66.42	8.40	9.23

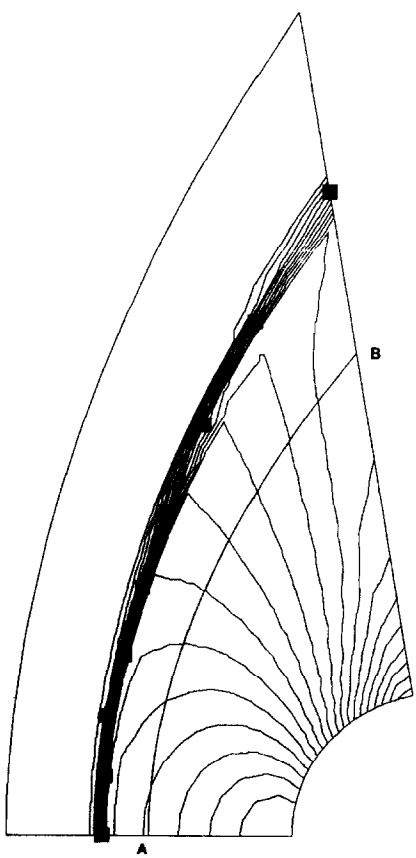

FIG. 10. Isobars at convergence, using the second-order Osher scheme.

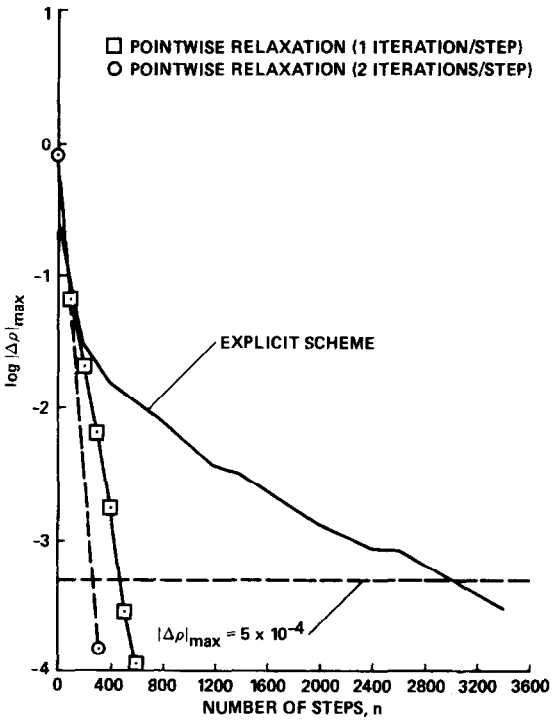

FIG. 11. Convergence history for the cylinder calculation (implicit point-wise relaxation and explicit second-order Osher-scheme calculations).

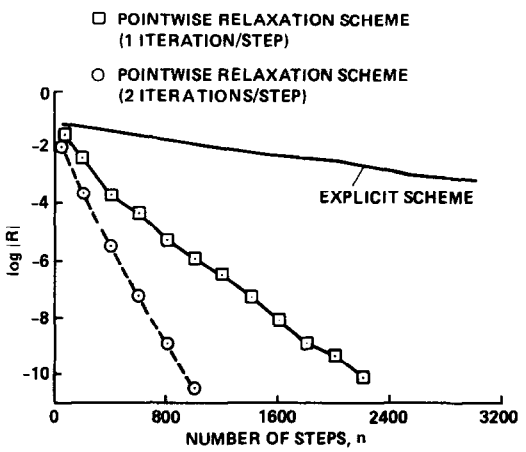

FIG. 12. Time history of the maximum residual in the continuity equation (second-order Osher scheme).

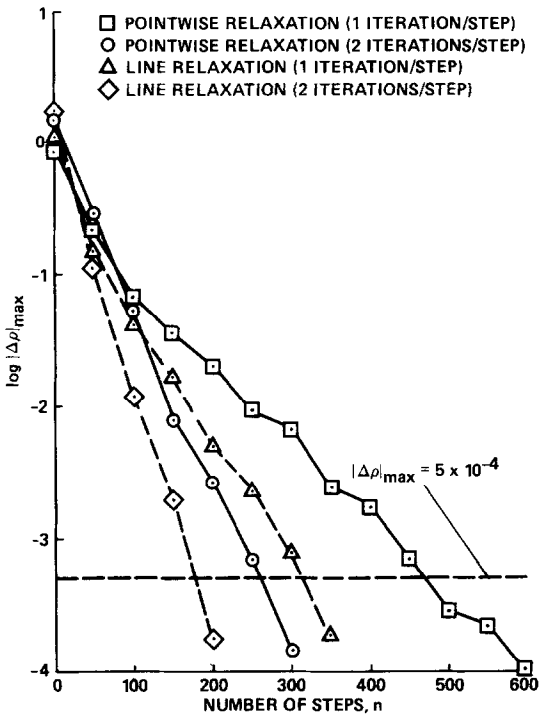

FIG. 13. Convergence history for the cylinder calculation (implicit point-wise and line relaxation second-order Osher-scheme calculations).

solution was approximately the same as that required for the one-iteration-per-step relaxation scheme. Figure 12 shows the time-variation of the magnitude of the maximum residue in the continuity equation (R) for the second-order accurate

To determine the convergence rates that can be obtained with other relaxation schemes, the preceding calculation was performed once again, but with a line-relaxation scheme. The choice of lines was alternated between the constant ξ- and the constant η-grid lines at each integration step. The scheme required 325 steps to converge when only one iteration was performed at each time-step and 172 steps when two iterations were used at each time-step. However, the computing time required to obtain the converged solution was approximately the same in both cases. It was also found that the point-wise relaxation schemes required about 25 % more computing time than the line-relaxation scheme to yield the converged solution.

A comparative study of the convergence histories for the point-wise and line relaxation schemes is shown in Fig. 13. It is clear that line relaxation with multiple iterations has the fastest convergence rate. However, it must also be remembered

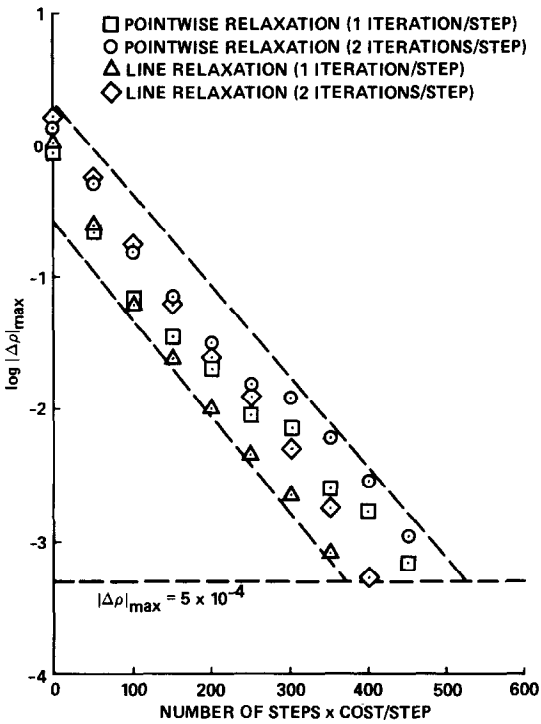

FIG. 14. Convergence history for the cylinder calculation with the integration step number modified to include computing cost.

that line-relaxation is more expensive than point-wise relaxation. Figure 14 is also a comparative study of convergence histories except that the integration step number has been multiplied by the computing cost per time-step (assuming the computing cost per time-step for the one-iteration-per step point-wise relaxation scheme to be unity). It can be seen from this figure that although the line-relaxation schemes are less expensive for the cases considered, data corresponding to all the relaxation

TABLE III

Computing Times for the Second-Order-Accurate Osher Scheme

Type of relaxation used	Point-wise	Point-wise	Line	Line
Number of iterations per step	1	2	1	2
Time per 100 steps, sec	3.77	7.46	4.56	9.02
Number of steps to converge	485	255	325	172
Time to converge, sec	18.30	19.02	14.83	15.51

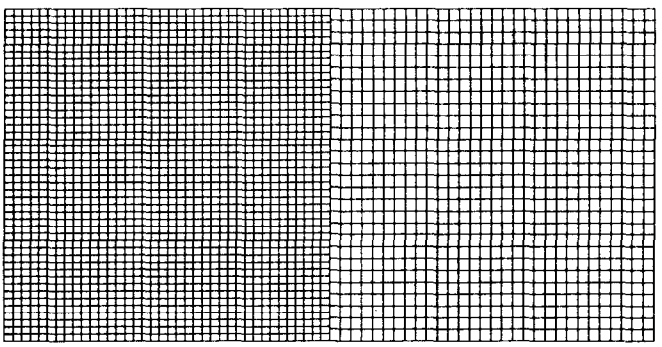

FIG. 15. Grid for the two-zone vortex calculations.

schemes fall within a narrow band. This signifies that there are no major computational advantages in using one scheme over another. However, the point-wise relaxation schemes are easier to program (especially for zonal calculations) and are highly vectorizable without requiring additional memory. Table III summarizes convergence rates and computing times for all the variants of the relaxation approach mentioned above.

Vortex Motion through a Zonal Boundary

Relaxation schemes as developed in Ref. [6] can be used effectively to obtain time-accurate solutions (in the past they were commonly resorted to only when steady-state results were required). The following example demonstrates this aspect of the relaxation scheme. The calculation consisted of a Lamb-type analytical vortex moving through a zonal boundary. It is possible to effect vortex motion either by superimposing a moving free-stream condition on the vortex (in which case the vortex is convected along with the fluid at the free-stream velocity), or by keeping the vortex stationary and by moving the grid. The two approaches yield identical results. In this study the vortex was initialized using the procedure given in [11],

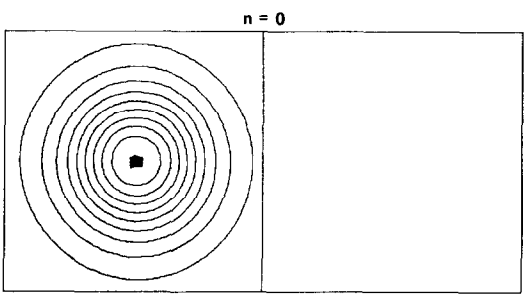

FIG. 16. Isobars for the vortex calculation (at initialization).

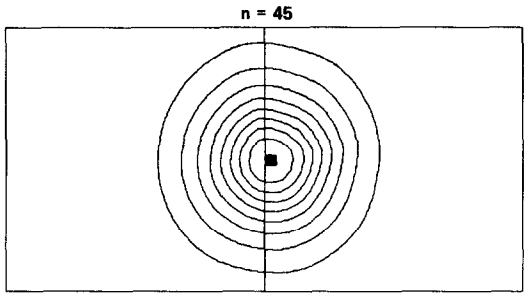

FIG. 17. Isobars for the vortex calculation (after 45 steps).

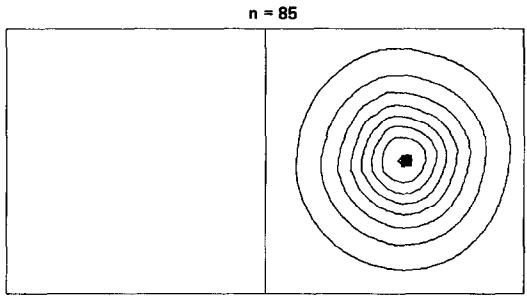

FIG. 18. Isobars for the vortex calculation (after 85 steps).

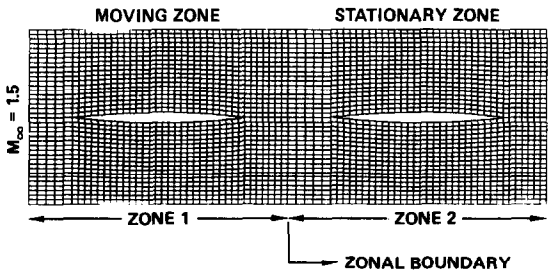

FIG. 19. Two-zone grid for the double-airfoil calculation.

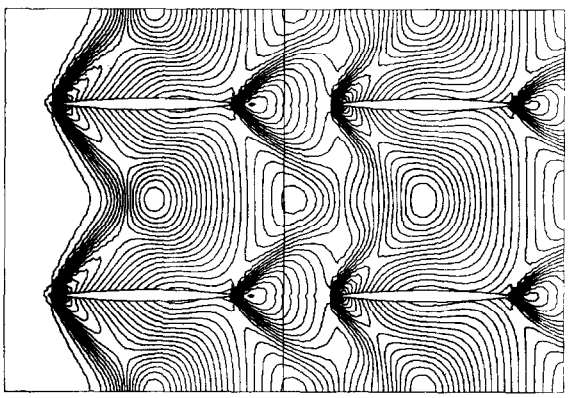

FIG. 20. Pressure contours at convergence for the double-airfoil calculation (both airfoils stationary).

and then the grid was moved at a constant speed in a direction opposite to the direction in which vortex motion was desired. Figure 15 shows the two-zone grid used for the calculation. Only the central portion of the flow field is presented in Figs. 15–18 since the essential features of the vortex are contained in this region. The discontinuous nature of the grid lines at the zonal boundary is evident. The calculation was performed with the second-order-accurate Osher scheme in conjunction with a line-relaxation technique. Four iterations were used at each time-step to obtain time-accurate results. The calculation was performed at a CFL number of 2.0.

Figure 16 shows pressure contours at initialization. The solid core at the center of the constant pressure circles in this figure and the following two figures is the analytical center of the vortex. Figure 17 shows pressure contours after 45 integration steps. The slope continuity of the contour lines across the zonal boun-

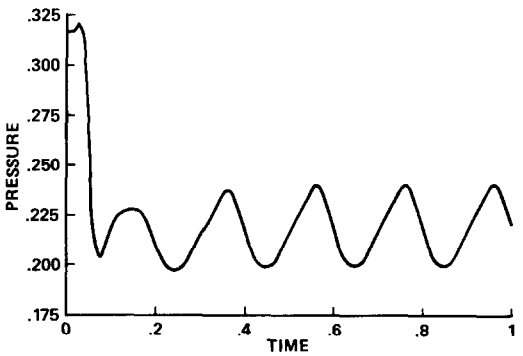

FIG. 21. Pressure history at midchord on the lower surface of the aft airfoil.

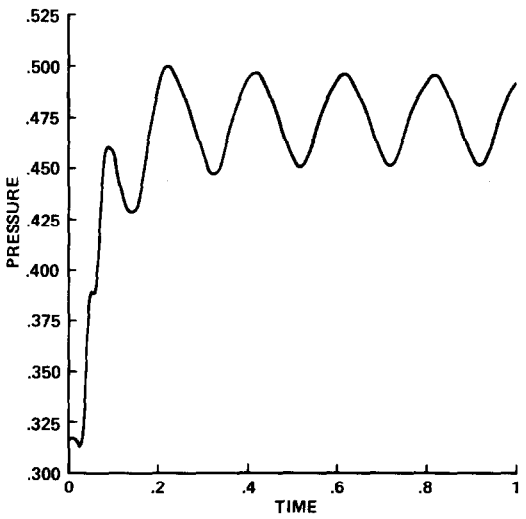

FIG. 22. Pressure history at midchord on the upper surface of the aft airfoil.

dary is clearly seen. The center of the circles coincides with the analytical center of the vortex (this demonstrates the time-accuracy of the zonal scheme). Figure 18 presents pressure contours obtained after 85 integration steps. The vortex has moved entirely into zone 2. The contours are circular and are not distorted (they are not as smooth as they are in Fig. 16 because of the coarser grid used in zone 2), and the center of the circles again coincides with the analytical center.

Time-Dependent Double-Airfoil Calculation

As stated earlier, one of the important applications of the zonal approach is the treatment of regions that contain parts that move relative to each other such as

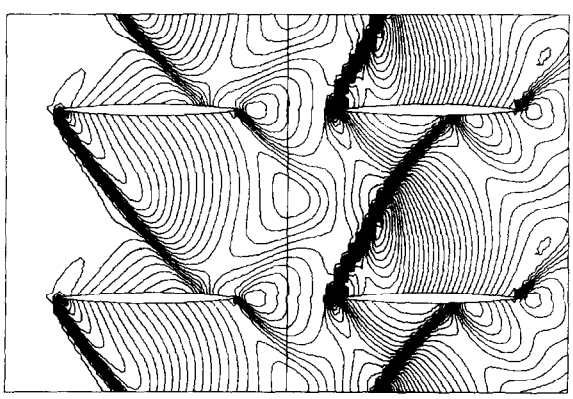

FIG. 23. Pressure contours after 1000 integration steps (4.0 cycles).

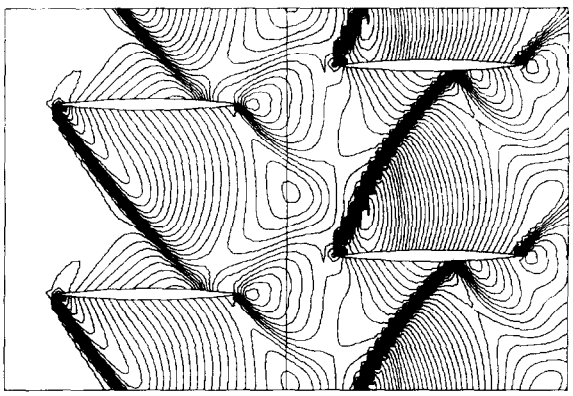

FIG. 24. Pressure contours after 1050 integration steps (4.2 cycles).

rotor–stator combinations in turbines. The following example was chosen to illustrate how one might perform such a calculation.

The configuration chosen consists of two parabolic-arc airfoils in a supersonic free stream ($M_\infty = 1.5$). Figure 19 shows the two-zone grid used to discretize the region of interest. Zone 2 is stationary (and so is the aft airfoil), and zone 1 is fixed to the first airfoil which moves in a downward direction. Although grid lines are continuous at the zonal boundary in Fig. 19, a discontinuity in grid lines will develop as the first airfoil and zone 1 move downward. The zonal-boundary points of zone 1 will slip past the zonal-boundary points of zone 2.

Periodic boundary conditions are imposed on the upper and lower boundaries of both the zones. Free-stream conditions are imposed on the left boundary of zone 1 and supersonic exit boundary conditions are imposed on the right boundary of zone 2. The implicit, zonal-boundary condition developed in this study is used at the boundary that separates the two zones.

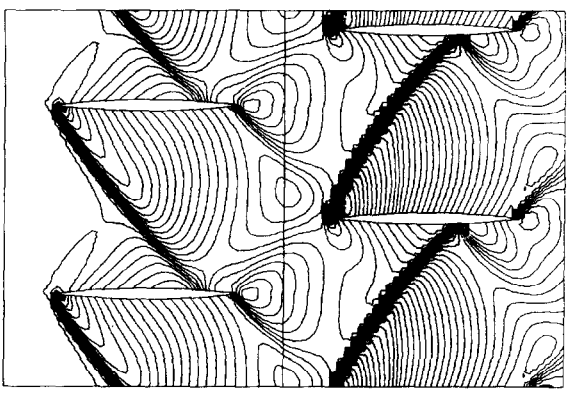

FIG. 25. Pressure contours after 1100 integration steps (4.4 cycles).

Figure 20 shows pressure contours obtained at convergence (both airfoils stationary) using the second-order-accurate Osher scheme. Although the calculation was performed with only two airfoils, for the sake of clarity this contour plot (and the following six contour plots) depicts four airfoils. The information regarding the additional airfoils is obtained from the periodicity condition. The point-wise relaxation technique was used for this calculation. The attached oblique shocks at the leading and trailing edges of both the airfoils and the expansion waves that emanate from the surfaces of the two airfoils are evident. The expansion waves impinge on the leading and trailing edge shocks and thus weaken them.

The first airfoil was then made to move with a contant downward velocity (the magnitude of the velocity corresponds to a Mach number of 0.1 with respect to free-stream conditions). The calculation was performed at a CFL number of approximately 2.0. At this CFL number, 250 integration steps were required for each cycle (one cycle corresponds to the motion of the forward airfoil from a given position relative to the aft airfoil to a similar position relative to the aft airfoil just below the first one). Approximately two cycles were required to establish periodicity of the flow in time. Figure 21 shows the surface pressure history at midchord on the lower surface of the rear airfoil. It can be seen that after the initial transients (which last for about two cycles) the surface pressure at midchord becomes periodic in time, thus demonstrating the capability of the relaxation zonal-scheme in simulating periodic time-dependent flow. Figure 22 shows the surface pressure history at midchord on the upper surface of the aft airfoil. The behavior seen in Fig. 22 is similar to that seen in Fig. 21 except for a phase shift and a difference in the mean value of the pressure. The mean value on the upper surface is higher than the steady-state pressure (when both the airfoils are stationary) whereas the mean value on the lower surface is lower than the steady-state pressure.

Figures 23–28 show pressure contours at various positions of the forward airfoil (with respect to the aft airfoil) as it moves downward. These contours were

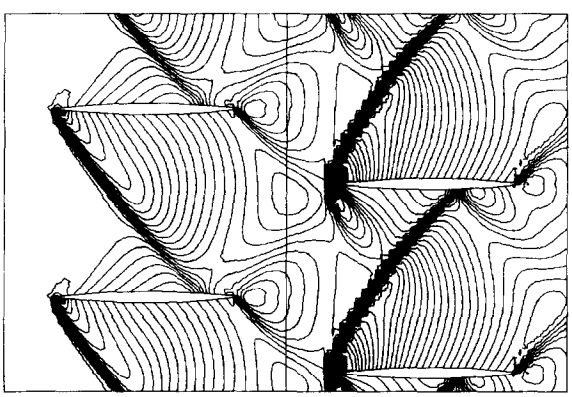

FIG. 26. Pressure contours after 1150 integration steps (4.6 cycles).

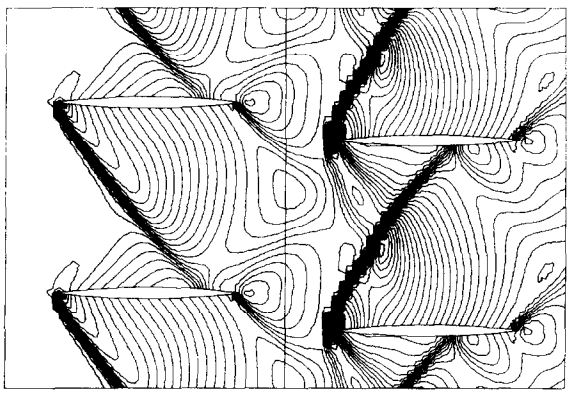

FIG.27. Pressure contours after 1200 integration steps (4.8 cycles).

obtained after the initial transients had subsided (the results correspond to the fifth cycle). The downward motion of the forward airfoil results in shocks at the leading and trailing edges on the lower surface of this airfoil. The flow is no longer symmetric as it is in Fig. 20. The motion of the forward airfoil and the flow associated with it create a changing upstream condition on the aft airfoil which in turn results in a cyclic time-dependent flow in zone 2. The interaction of the trailing-edge shock of the forward airfoil with the leading-edge shock of the aft airfoil is clearly seen. The periodicity of the flow in time is also evident in Figs. 23 and 28. The positions of various contour levels in these two figures are identical (in fact they are superimposable). One aspect of rotor–stator configurations that is not represented in the present calculation is the effect of the aft airfoil on the forward airfoil (the supersonic nature of the flow does not permit such an interaction). However, the zonal

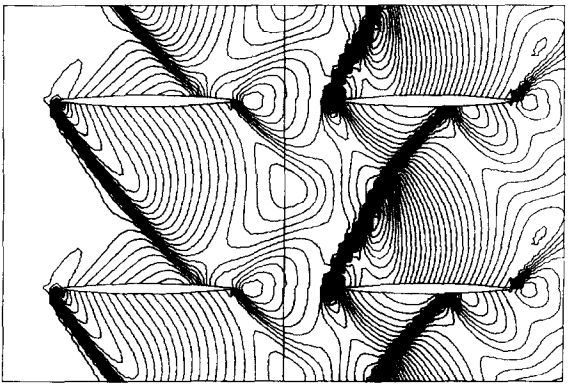

FIG. 28. Pressure contours after 1250 integration steps (5.0 cycles).

boundary conditions have been implemented so that an interaction, if present, will be accurately treated. A calculation that demonstrates the capability of the present zonal scheme in accurately simulating such an interaction is presented in Ref. [12].

CONCLUSIONS

A conservative zonal scheme that permits calculations on several grids that are patched together and that can be used in conjunction with explicit integration schemes (applied to the Euler equations) has been extended so that it can be used with implicit, relaxation schemes. Considerable increases in convergence rates have been demonstrated with the implicit, relaxation-zonal scheme (when compared to the explicit scheme).

Results in the form of pressure contours are presented for inviscid supersonic flow over a cylinder. The calculation was performed on two grids patched together at a zonal boundary. The contours are continuous across the zonal boundary and the bow shock was observed to move freely from the first zone to the second even at a CFL number of 500. The use of the implicit, relaxation scheme was found to reduce the computing time by approximately a factor of 5 (compared to the explicit scheme). Unlike the implicit, factored zonal scheme [3], the relaxation zonal scheme was found to be stable even at large CFL numbers of the order of 5000. However, the rate of convergence reached an asymptotic value with increasing CFL number. The zonal-boundary condition was simpler to program for implicit, relaxation schemes than it was for implicit, factored schemes.

Results that demonstrate the time accuracy of the present zonal scheme and the

problems such as rotor–stator interaction and helicopter rotor–fuselage combinations. In the case of the double airfoil calculation (chosen to model a rotor–stator configuration), the capability of the zonal scheme in simulating periodic, time-dependent flow is clearly observed.

REFERENCES

1. M. M. RAI, K. A. HESSENIUS, AND S. R. CHAKRAVARTHY, *Comput. and Fluids* **12**, 3 (1984).
2. M. M. RAI, *J. Comput. Phys.* **62** (1986).
3. M. M. RAI, AIAA Paper 85-0488, Reno, NV, 1985.
4. R. M. BEAM AND R. F. WARMING, "Proceedings of the AIAA 3rd Computational Fluid Dynamics Conference," Albuquerque, NM, 1977.
5. M. M. RAI AND S. R. CHAKRAVARTHY, AIAA Paper 84-0088, Reno, NV, 1984.
6. S. R. CHAKRAVARTHY, AIAA Paper 84-0165, Reno, NV, (1984).
7. J. L. STEGER AND R. F. WARMING, *J. Comput. Phys.*, **40** (1981).
8. P. L. ROE, *J. Comput. Phys.* **43** (1981).
9. S. R. CHAKRAVARTY AND S. OSHER, AIAA Paper 83-1943, Danvers, MA, 1983.
10. A. N. LYUBIMOV AND V. V. RUSANOV, NASA TT-F 715 (1973).
11. G. R. SRINIVASAN, W. J. MCCROSKEY, AND P. KUTLER, AIAA Paper 84-0254, Reno, NV, 1984.
12. M. M. RAI, AIAA Paper 85-1519CP, Cincinnati, OH, 1985.